ELSEVIER

Journal of Electron Spectroscopy and Related Phenomena 84 (1997) 171–188

JOURNAL OF ELECTRON SPECTROSCOPY and Related Phenomena

Recent progress in photoemission microscopy with emphasis on chemical and magnetic sensitivity

W. Swiech[a,*], G.H. Fecher[a], Ch. Ziethen[a], O. Schmidt[a], G. Schönhense[a], K. Grzelakowski[b], C. M. Schneider[c], R. Frömter[c], H.P. Oepen[c], J. Kirschner[c]

[a]*Institut für Physik, Staudinger Weg 7, Johannes Gutenberg-Universität Mainz, D-55099 Mainz, Germany*
[b]*FOCUS GmbH, Am Birkhecker Berg 20, D-65510 Hünstetten, Germany*
[c]*Max-Planck-Institut für Mikrostrukturphysik, Weinberg 2, D-06120 Halle/Saale, Germany*

Received 8 January 1996; accepted 22 December 1996

Abstract

With the improved access to synchrotron radiation sources photoemission electron microscopy is developing into a versatile analytical tool in surface and materials science. The broad spectral range and the well-defined polarization characteristics of synchrotron light permit a unique combination of topographic, chemical, and even magnetic investigations down to a mesoscopic scale. The potentiality of photoemission electron microscopy is demonstrated by several experiments on surfaces and microstructured thin film systems, which have been carried out with a newly designed instrument. We discuss its different modes of operation with respect to both microscopy and spectroscopy. A combination of elemental selectivity and magnetic sensitivity is achieved by using circularly polarized soft X-rays and exploiting the effect of magnetic circular dichroism. This way one obtains information about the magnetic state of individual chemical components within the sample. © 1997 Elsevier Science B.V.

Keywords: Photoemission microscopy; Surface magnetism; Spectromicroscopy; Microspectroscopy

1. Introduction

Conventional photoemission electron microscopy (PEEM) using a laboratory ultraviolet lamp as an illumination source and an immersion objective lens as the first part of the electron-optical column was invented already in the 1930s [1]. It is now becoming one of the important mesoscopic imaging techniques for surface physics or chemistry and in biology. This is due to the fact that it fills the gap between optical microscopy and scanning probe microscopy, as e.g. STM or AFM, if the balance between high lateral resolution and size of the field of view is considered. During the last decade, PEEM instruments of various designs have been utilized among others to study such phenomena as adsorption of metallic ultrathin films [2–5], microtopography of metal and semiconductor surfaces [6,7], spatio-temporal pattern formation and front propagation occuring during surface reactions of heterogeneous catalysis [8–14], surface diffusion of gases [15–17] and metals [18–20], diamond growth on metals and semiconductor surfaces [21–23], biological samples [24–26], etc.

One of the important features of an immersion lens PEEM is its parallel mode of image formation, i.e. all pixels of an image are acquired simultaneously.

* Corresponding author.

PII S0368-2048(97)00022-4

Hence, high temporal resolution becomes possible provided the illumination flux density is sufficiently high. However, although a PEEM can be readily implemented in an experimental set-up, its applicability with laboratory UV-sources remains relatively limited. This is due to the fact that the main contrast mechanism—when exciting electrons from the vicinity of the Fermi level—is the work function contrast. In this way the range of applications becomes restricted due to the substantial lack of straightforward and unambiguously interpretable information about the chemical nature of the objects of interest. This limitation can be overcome by increasing the photon energy of the illumination beam, thereby gaining access to well established techniques such as ultraviolet electron spectroscopy (UPS), X-ray photoelectron spectroscopy (XPS), X-ray absorption spectroscopy (XAS) or photon induced Auger electron spectroscopy (AES) which can now be performed simply by using an immersion objective PEEM.

Information on the spatial distribution of the electronic structure, chemical nature, or the local magnetization at surfaces can thus be obtained [27]. Of importance in this respect is the excitation with synchrotron radiation. Dedicated beam lines with high brilliance, variable photon polarization (both linear and circular) and broad energy range have become recently available in several facilities. It is the tunability of the exciting radiation which is of primary importance, since it allows one to easily adjust the energy of illumination to specific core levels or select appropriate Auger transitions. By means of a suitable electron-optical device it becomes rather straightforward to map the abundance of different chemical species at the sample surface. Two approaches have been established. The first one is called ''microspectroscopy''. It consists of the acquisition of ''local'' electron spectra from small areas on the sample surface either by sweeping the primary photon energy and collecting the secondary electron yield, or keeping the illumination energy fixed and ramping an (optional) band-pass energy analyzer in order to select electrons with a specific kinetic energy. The first approach exploits the information contained in XAS and can be realized with a rather simple PEEM that is not equipped with any energy spectrometer. In combination with a small spot imaging analysis system one achieves a parallel, i.e. simultaneous acquisition of spectra from different regions of interest on the sample surface. In this way, using XAS an elemental feature recognition or even mapping of the surface area can be performed. In the following, we will refer to such an approach as to ''micro-XAS''. The identification of elements is due to the mere presence of Auger- or secondary electrons excited from a given core level. Micro-NEXAFS (near-edge X-ray absorption fine structure) becomes possible in a similar manner, too.

When the illumination energy is set to a given absorption edge corresponding to a core level of the element under consideration, high resolution microimages can be acquired. They reveal the spatial distribution of this element. This approach is termed ''spectromicroscopy''. It is worth mentioning that it can still be performed in a PEEM without any energy analyzer. It is essentially due to the fact that the immersion lens together with the contrast aperture located in the back focal plane of the objective acts as an effective low pass energy filter and thereby limits the energy spread of the electrons forming the image. The aperture is therefore mandatory to obtain a high lateral resolution of the microscope despite the electron-optical aberrations. Hence, such a simple PEEM images practically only with secondary electrons. It is due to the fact that in the soft X-ray range, the main decay channel following excitations from core-levels to the states above Fermi level is the production of Auger electrons, which subsequently create a secondary electron cascade [28]. This ''amplification'' process ensures that images can be recorded with a high signal level.

Compositional or chemical contrast results from local variations of the emission intensity due to differing photoabsorption cross-sections or X-ray absorption coefficients [29]. The latter is in general strongly energy dependent, and an instrument operated in this specific mode may be called an X-ray secondary emission microscope (X-SEM) [30]. There is one more important feature of the immersion objective lens. Due to parabolic trajectories of the accelerated electrons the acceptance angle in a PEEM is much higher than in any ''field-free'' entrance of a conventional energy analyzer. This will significantly increase the signal. An obvious disadvantage of such an micro-XAS approach is that not all the absorption edges

accessible with a given monochromator have the same transition strength. The weaker ones may yield only a poor signal-to-noise ratio, thus precluding the acquisition of meaningful micrographs.

A PEEM operated without energy filtering is limited to the use of XAS as a spectroscopic source of information. Further excitation channels become accessible, however, if the instrument is equipped with an imaging or band-pass filter. In this case one can acquire images at energies corresponding to characteristic photoelectron or Auger electron lines and perform laterally resolved XPS and AES. Recently, substantial construction efforts have been undertaken in order to design such filters as 90° or 180° electrostatic prisms ([31–33] and see this issue), Omega magnetic filter ([34–36] and see this issue), or crossed field electro-magnetic Wien filter [37], also in a multipole version [38,39]. Besides spectromicroscopy where series of microimages are acquired as spatial distributions of features visible at given photoelectron or Auger electron energies, also microspectroscopy can be easily operated by continuously ramping the energy window of the filter and collecting the signal from the chosen portions of the image at fixed photon energies. Such an instrument can be called X-ray PEEM or Auger emission electron microscope (AEEM) [40]. Again, one can take advantage of a small spot image analysis system to acquire simultaneously AES, XPS or even UPS spectra from many areas on the sample surface. PEEM instruments both backed with an imaging energy filter and also without energy selection (i.e. operating on the basis of XAS) have been successfully applied to studies of surface oxidation [30,41,42], biological and neurobiology toxicology [43–45], small particle (or microprecipitate) recognition [46], hazardous materials [47], polymers [46], high temperature superconductors [48–50] and magnetic domain imaging [27,51,52]. More information can be found in recent review articles [46,53,54].

In the following we will report on the application of a novel PEEM instrument (a so-called integral sample stage PEEM) to chemically selective and magnetization sensitive studies. This instrument can be operated in two modes. In the XAS mode, images containing chemical and magnetic information are obtained by exploiting the tunability and polarization characteristics of synchrotron radiation. The experiments were carried out at the German synchrotron radiation facility BESSY in Berlin, employing the beamline SX700/3 with circularly polarized radiation in the energy range 50–1000 eV. As an approach to the direct photoemission or ESCA mode, we introduced a non-imaging energy filter, which used the excellent imaging properties of the PEEM optics to permit the acquisition of small spot photoelectron and Auger electron spectra even with a conventional electron gun or laboratory X-ray source. This hybrid design thus combines the advantages of an XAS PEEM and an electron spectrometer.

This paper is divided into the following sections: Section 2 describes technical features of the instrument. Section 3 and Section 4 are dedicated to microspectroscopy and spectromicroscopy, respectively. Results of magnetization sensitive imaging are reported in Section 5. First results using a non-imaging energy analyzer for micro-ESCA applications are discussed in Section 6.

2. Technical features of the microscope

2.1. Principle of a photoelectron emission microscope

A photoelectron emission microscope (PEEM) essentially consists of an imaging electrostatic electron lens system and a UV light source for the generation of photoelectrons via photoemission. The basic principle is as follows: the photoelectrons emitted from the surface are imaged onto a channel plate for intensification and finally onto a fluorescent screen for direct inspection or observation using a CCD camera. In contrast to a scanning electron microscope (SEM), the PEEM does not use a scanned probe beam, but the sample surface is uniformly illuminated by, e.g. UV light in laboratory applications. In this way any probe-induced damage of sensitive surfaces or adspecies which frequently occurs in an SEM is largely reduced. The magnified image of the surface can be observed directly and in real-time (even with video frequency, if the photon intensity is sufficient) on the fluorescent screen.

With respect to its parallel image acquisition, the basic principle of operation is similar to an optical microscope. However, since electrons are used for

imaging the resolution is no longer diffraction-limited by the wavelength of the photons. The optical analogy carries even further to the objective lens. Electrons emitted by UV light, say $\hbar\omega = 8$ eV, have a certain energy distribution cut off by the work function, resulting in a rather low ($\approx$ 1–2eV) average kinetic energy. Due to the chromatic aberration of the objective lens, the energy spread directly affects the achievable lateral resolution. In order to reduce the influence of the chromatic aberration, a high electrostatic field in front of the sample accelerates the released electrons to energies of typically 10 to 15 keV. As a convenient side effect, electrons from a larger solid angle contribute to the image, thus reducing the acquisition time. This lens system is the electron-optical counterpart to immersion lens objectives used in optical microscopy and permits a lateral resolution of less than typically 30 nm.

The contrast observed in a PEEM image obtained using UV light results from spatial variations of the electron yield as a consequence of lateral variations of the work function as well as surface topography. Work function variations can be of a chemical nature, e.g. adsorbates causing a work function difference compared to the uncovered substrate, different crystallographic orientations, reduced work function at steps and defect sites, etc. Topographic contrast arises from shadowing, different emission angles, etc. In the past, numerous studies in surface chemistry and thin film growth have been conveniently carried out by means of commercially available UV lamps, such as mercury, xenon, or deuterium discharge sources.

With the development of dedicated synchrotron radiation facilities, intense light of higher photon energies in the vacuum ultraviolet (10 eV $< \hbar\omega <$ 30 eV) and soft X-ray regime (30 eV $< \hbar\omega <$ 1 keV) is now readily available. In addition, synchrotron radiation has unique properties with respect to its polarization which may be linear or even circular. These properties introduce a variety of new contrast mechanisms into the field of photoemission microscopy. By using soft X-rays, for instance, characteristic core-levels become accessible and permit "element specific" imaging. For polarized photon beams, magnetic circular or linear dichroism can be exploited in order to image "magnetic microstructures" with high lateral resolution ("domain imaging"). Examples for the application of all these techniques will be discussed in the following sections.

2.2. A new PEEM with an integral sample stage

The studies described in this contribution used a photoelectron emission microscope with integrated sample stage (referred to henceforth as IS-PEEM). The instrument was developed, designed, and constructed by FOCUS GmbH (Germany). The IS-PEEM is a three-lens electrostatic straight microscope (Fig. 1). In the current version, it comprises an electrostatic tetrode objective lens, a contrast aperture located in the back focal plane (with piezomotor-driven aperture exchange and adjustment), an octopole stigmator/deflector for maximum resolution, a continuously variable iris aperture located in the first image plane for enhancement of contrast and resolution, background reduction in high-resolution mode as well as area selection for micro-analysis, and two projective lenses. The lateral electron distribution is intensified by a multichannel plate and made visible by a fluorescent screen (YAG crystal). Fig. 1 shows a

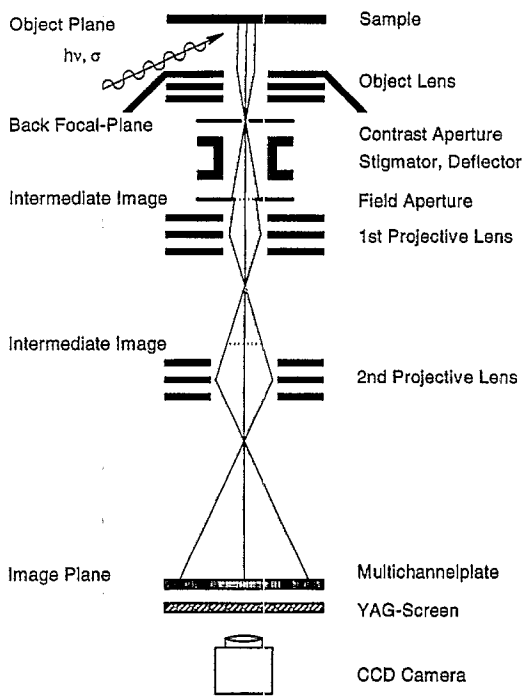

Fig. 1. Schematics of the novel integral sample stage photoemission electron microscope (IS-PEEM).

rough schematic (not to scale) illustrating the principal arrangement.

A key feature of the IS-PEEM is the integral sample stage with piezoelectrically driven sample positioning. It forms one building unit with the body of the objective thus effectively avoiding any possible relative motions of sample and objective which could otherwise impair the image quality. This is a particular advantage considering the vibrational problems usually arising from a separately mounted sample manipulator, and allows for optimum magnetic shielding of the space between specimen and objective lens [55]. The distance between the sample plane and the objective can be accurately preadjusted thus avoiding time-consuming in-situ adjustment. Each sample is mounted on a standard support which can be easily transferred into and out of the sample stage by means of a wobble-stick. Once inserted in the sample stage, lateral positioning of the sample in front of the objective is only done by the piezoelectric drives. These permit a scan range of approximately 5 mm × 5 mm.

The requirements for a well defined field between sample and objective also impose some restrictions on the shape of the sample. The sample surface should be as flat a possible. Small samples may create problems in this respect because of the field inhomogeneities at the sample edges. In this case we covered the sample by an electropolished cup with a flat top formed out of a thin Mo or Ta sheet. The cup carried a circular hole the size of which was chosen to mask most of the sample edge.

The IS-PEEM is further equipped with a continuously variable iris aperture which can be adjusted in UHV by means of a rotary motion feedthrough on the base flange. Since the iris is located in the plane of the first image or intermediate plane produced by the objective lens, its hexagonal shape appears on the fluorescent screen after being magnified by the projective lenses (the iris may thus be used as an easy reference for the intermediate plane during adjustment of the lenses). When being closed, it acts as an efficient sample microspot selector, because both the image of the sample surface and the image of the hexagonal shape of the iris in the intermediate plane are simultaneously focused onto the screen. This "microspot selector" allows one to select well defined sample areas of down to about 1 μm dia. for microspectroscopy purposes. A straightforward application of this operational mode is, for example, X-ray absorption spectroscopy (micro-XAS) by varying the excitation energy. By introducing an additional energy filter into the electron beam also Auger electron spectroscopy (micro-AES) or micro-ESCA becomes possible. Furthermore, the iris aperture serves as a means for a general enhancement of contrast and resolution as well as background reduction especially in the high-resolution mode.

The contrast aperture of the IS-PEEM is located in the back focal plane of the objective lens. The diameter of the contrast aperture determines both the resolution of the instrument (through the spherical and chromatical aberration coefficients) and also the intensity of the image (through its cross-section). Hence it is very advantageous, to be able to select different sizes of the contrast aperture in-situ during the experiment, thus optimizing the interplay between spatial resolution and image intensity (analogously to the selection of the slit-widths of a spectrometer). In the IS-PEEM an in-situ selection of various contrast apertures is realized by a piezomotor-driven multi-aperture mount. Five different sizes can thus be easily and rapidly selected. Besides the size selection there is another advantage of the piezomotor movement facility of the contrast aperture: The position of the aperture relative to the beam axis can be varied, which allows to make use of "orientational contrast" or contrast enhancement, e.g. through Lorenz force in magnetic imaging. The orientational contrast arises in off-axis position of the contrast aperture and resembles the influence of sample illumination in optical microscopy and of sample rotation in scanning electron microscopy (SEM).

In order to reach the ultimate resolution every electron microscope must be operated with a stigmator which corrects non-spherical aberrations of the optics. The IS-PEEM uses an electrostatic octopole stigmator located in the back focal plane of the objective lens. The octopole arrangement ensures that astigmatism can be corrected in any rotational orientation, independently in the x/y orientation as well as in the $xy/-xy$ orientation (i.e. along a direction rotated by 45° with respect to x/y). In addition, the octopole can be used as an x/y deflector in order to shift the field of view without moving the sample. This can be useful for fine adjustment of the sample

position as well as for optimization of the focusing of the field of view (compensation of small misalignments of the sample).

The final electron distribution is intensified by a multichannel plate having a special thickness of 800 μm and converted into visible light by means of a YAG single-crystal fluorescent screen. Because of the array-structure of a multichannel plate and the limited size of a channel (typically $\approx$ 10 μm dia.), the image is patterned into small spots during the amplification process. This patterning determines the lateral resolution of an individual point (point resolution). As compared to double channel plate (''chevron'') arrangements, a dedicated single plate causes significantly less decrease of the point resolution. The ultimate lateral resolution of the instrument can thus be reached by a plate of only 20 mm dia. which is less fragile and much less sensitive to the humidity of ambient air than larger plates. In addition, the use of a single-crystal fluorescent screen further keeps the influence of the spot-resolution in the imaging device small, because there are absolutely no effects of grains of the fluorescent material (in contrast to conventional screens).

In our applications, two types of camera systems have been used for image acquisition. In a typical topography investigation (e.g. work function contrast using a Hg source) at moderate lateral resolution the image is easily visible with the bare eye and can be photographed similar to the one a LEED screen. A simple CCD video camera with 8-bit depth is sufficient to make such images visible on a monitor or take data in real time using a video recorder. For high-resolution imaging or applications of synchrotron radiation etc., a time integrating slow-scan Peltier-cooled CCD camera with 12-bit depth has been employed. The 12-bit images are captured by a frame grabber and read into a computer system for storage and further processing.

3. Microspectroscopy (chemical microanalysis) using tunable synchrotron radiation

In the following, we will discuss some microspectroscopy experiments which have been carried out using the IS-PEEM and soft X-ray radiation from a storage ring. In principle, two different spectroscopy modes can be considered: (i) electron emission spectroscopy in which electrons are analyzed according to their kinetic energy at a fixed excitation energy (cf. Section 6), and (ii) absorption spectroscopy in which the excitation energy is varied. In both cases, the variable iris aperture of the IS-PEEM may be conveniently used to select a well-defined microspot on the sample surface.

The general procedure for an absorption-type microspectroscopy experimental (μ-XAS) with the IS-PEEM is as follows: first the region of interest (e.g. an unknown chemical structure) is centered on the screen with the iris being opened, then the iris is closed down to the desired size such that only electrons from the region of interest can arrive at the fluorescent screen. Now the photon energy $\hbar\omega$ of the monochromator is tuned across characteristic electronic levels of the sample and simultaneously the intensity of the light spot on the screen is monitored (e.g. by using a CCD camera, photometer etc.). The plot of the intensity on the screen vs. photon energy yields the local absorption or emission spectrum of the selected microspot on the sample. It thus gives information on the local elemental distribution within the microspot. Note that for an electron emission spectroscopy an additional energy-dispersing element is needed in order to select the kinetic energy of the electrons. This can be, for example, a small electrostatic capacitor which is inserted into the beam behind the iris aperture (cf. Section 6).

In the case of X-ray absorption spectroscopy we employed an alternative approach which has the advantage that the spectroscopic information from several μm-sized regions can be obtained simultaneously. The regions are selected by means of a software-based small spot analysis system [56]. Examples of X-ray absorption (XAS) microspectra obtained in this manner are given in Fig. 2. The sample was a Permalloy ($Fe_{19}Ni_{81}$) pattern that has been deposited onto a silicon substrate. The resulting Permalloy squares have a size of about 20 $\times$ 20 μm and were 25 nm thick. The entire sample was initially covered with a 10 nm thick Au protective layer that was subsequently sputtered off in-situ.

The image (Fig. 2(a)) was acquired with the photon energy tuned to the Fe L_2 absorption edge ($\hbar\omega$ = 706.8 eV). Contrary to the simple expectation, the Permalloy squares appear darker than the Permalloy-free

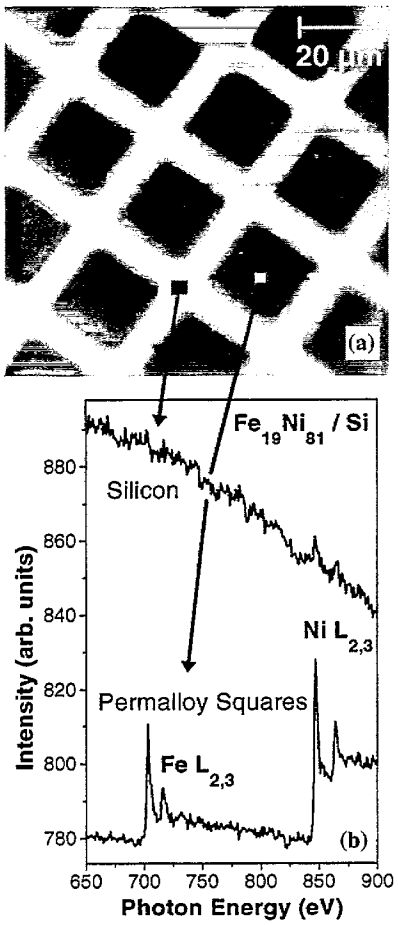

Fig. 2. Spectroscopic microscopy with the IS-PEEM without energy filter. (a) Microimage of a permalloy square (20 × 20 μm) array taken with the photon energy being tuned to the Fe L_3 absorption edge. Microspots where the spectra shown in (b) were acquired are shown to scale. (b) X-ray absorption spectra in the energy range of Fe and Ni $L_{2,3}$ absorption edges. They were acquired from the microspots located on a permalloy square and the initially uncovered Si surface between two adjacent squares, respectively. The intensity scale is the same for both spectra.

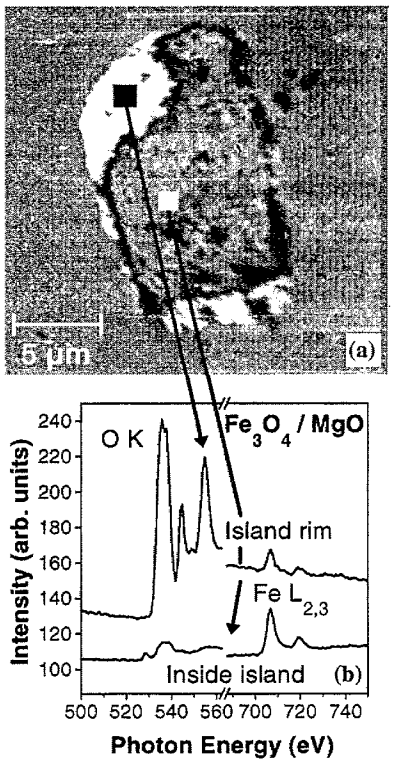

Fig. 3. An inhomogeneity or microprecipitate island in a continuous magnetite film evaporated onto a magnesium oxide substrate. (a) micrograph taken at a photon energy corresponding to the Fe L_3 absorption edge. Areas were the spectra shown in (b) were acquired are shown to scale. (b) Small spot X-ray absorption spectra taken on the island rim and within the island, respectively.

silicon bars. The reason for this is revealed by the micro-XAS spectra taken simultaneously from a selected area on the bright grid and on one of the dark squares (Fig. 2(b)). The spectra on the Permalloy square clearly show the Fe and Ni $L_{2,3}$ absorption edges, whereas the grid exhibits an almost featureless spectrum. At the position of the Fe L_3 absorption edge, where the image was taken, however, the absolute low-energy secondary electron yield (which constitutes the signal observed with a PEEM) from the Si substrate is higher than that from the Permalloy square, thus giving rise to a seemingly reversed contrast.

Looking closer at the XAS-spectrum from the Si substrate we note a small signal at the Ni $L_{2,3}$ edges. This indicates that a significant amount of nickel has diffused on the nominally Permalloy-free silicon bars. This may be due to a thermal treatment of the sample after growing the Permalloy microstructure. Because of the smaller concentration of Fe in the alloy, the corresponding Fe signal is weaker and masked by the statistical scatter of the data points so that no conclusions can be drawn on the Fe diffusion in this case.

Results for a different system are shown in Fig. 3. This sample was a thin magnetite film (Fe_3O_4) grown on the (100)-face of a MgO single crystal platelet.

(At Philips Research in Eindhoven Fe_3O_4 layers with a thickness of 500 Å were grown by molecular beam epitaxy (MBE) on MgO(100) substrates. The Fe_3O_4 layers were deposited by electron beam evaporation from an Fe target. During growth, a substrate temperature of 225°C was used and the oxygen pressure was maintained at 2.8×10^{-5} mbar. The handling after the growth which included a number of sputtering and annealing treatments caused defects on the otherwise flat Fe_3O_4 surface.) The film was smooth over most of the surface area, with only a few small defects or microprecipitates. One of them is imaged in Fig. 3(a). From topography studies it appears to be somewhat higher than the surrounding area and is therefore referred to as an "island". The image was taken at a photon energy corresponding to the Fe L_3-edge and one can clearly discern areas with different (dark and bright) contrast. The chemical composition of these areas can again be deduced from the local absorption spectra. In the center of the island we find iron (Fe $L_{2,3}$-edges) and oxygen (O K-edge) in relative concentrations compatible with magnetite. In the bright areas along the circumference of the island there is somewhat less iron, but a large signal from oxygen. This suggests that the Fe_3O_4 coverage at these regions is much thinner and the oxygen signal comes mainly from the MgO substrate. A possible explanation for the above findings could be that the smooth film is disrupted and a small Fe_3O_4 flake is peeling off the MgO substrate.

These examples demonstrate only one type of microspectroscopy experiment that can be performed with a photoemission microscope. In favorable cases one is not limited to the simplest form of XAS, but may even perform a microspot EXAFS (extended X-ray absorption fine structure), provided the brightness of the photon beam is sufficient. By picking out individual grains, this allows the study of local atomic arrangements even in polycrystalline materials. In conventional macroscopically integrating techniques one always has to worry about averaging effects brought about by different crystallographic orientations within the sampled region.

4. Element-specific imaging

The characteristic structure of an X-ray absorption spectrum (cf. Section 3) is not only extremely useful for chemical spot-analysis, but can also be conveniently employed in element-specific imaging. In this mode of operation images taken at well-defined excitation energies are compared. When the photon energy is tuned to the maximum of an absorption edge of a certain element, this element will appear bright ("light up") in the image. Thus its lateral distribution becomes visible on the screen. The "background" of electron emission corresponding to all lower-lying photoabsorption edges can easily be subtracted by taking a second image at a photon energy immediately below the edge (I_b) and subtract this image pixel-by-pixel (x,y) from the original (I_a)

$$I_d(x,y) = I_a(x,y) - I_b(x,y) \quad (1)$$

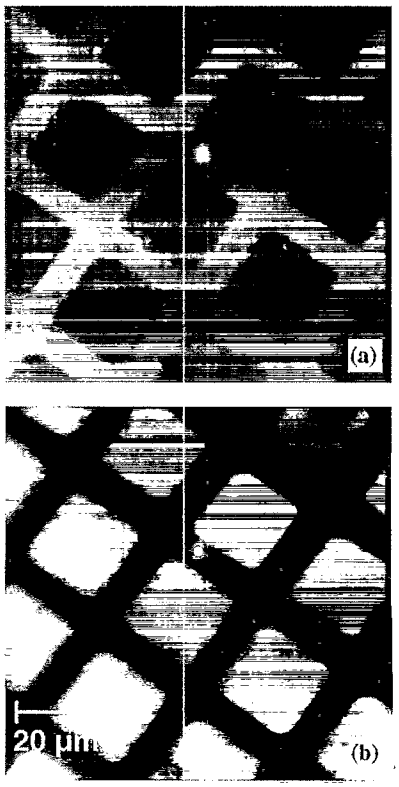

Fig. 4. Elemental mapping of the Permalloy microstructure. (a) Micrograph taken with the photon energy being tuned to the Ni L_3 absorption edge. (b) Pixel-by-pixel difference image of micrographs taken at the Ni L_3 edge and 5 eV below the absorption edge, respectively. In this way, the topographic features are canceling out. The image contains solely information on the spatial distribution of Ni.

The resulting difference image I_d directly shows the distribution of the selected element. In order to preserve the lateral resolution during this digital subtraction method, it is mandatory to suppress any sample drift or vibrations between the acquisition of the two images I_a and I_b. The unique IS-PEEM design with its integral sample stage ensures the stability of the sample position required for this application.

At the maximum of the absorption edge the kinetic energy of the corresponding photoelectrons is small, thus the electron optics is adjusted to the low-energy maximum of the energy distribution. Note that direct transitions from all higher-lying core levels of all elements present in the sample will generate electron signals at higher kinetic energies. These electrons can cause a diffuse (non-focused) background in an individual image. It cancels, however, in the difference image I_d.

In order to demonstrate the operational mode of chemically selective imaging we turn back to the samples discussed in Section 3. The image from the Permalloy pattern shown in Fig. 4(a) has been recorded at the Ni L_3-edge (it corresponds to I_a in eqn (1)). It shows a reversed contrast similar to Fig. 2(a). The difference in the contrast levels is significantly smaller than in Fig. 2(a), because the absolute signal heights from the Permalloy squares and the Si stripes at this photon energy ($\hbar\omega$ = 852.7 eV) are almost comparable (Fig. 2(b)). But still the Si substrate appears slightly brighter than the Permalloy pattern. This changes, however, when we form a difference image according to the above prescription. For this purpose, the second image I_b was acquired at $\hbar\omega$ = 847 eV, i.e. in front of the Ni L_3-edge. In the resulting difference image (Fig. 4(b)) the Permalloy squares now appear bright on a dark background, directly reflecting the lateral abundance of the element Ni. A similar result was obtained for iron by subtracting images at and in front of the Fe L_3 absorption edge. We would like to point out that the typical acquisition time for a single image was of the order of minutes. Thus chemically selective images with a good lateral resolution and signal-to-noise ratio can be obtained rather quickly.

In a similar manner we can map the distribution of oxygen and iron in the magnetite film shown in Fig. 3(a). The difference images for the Fe L_3 (Fig. 5(a)) and the O K-edge (Fig. 5(b)) exhibit an almost inverted contrast pattern. We find a homogeneous distribution of iron outside the defect. Even within the defect there is a relatively large area with a comparable Fe signal. With respect to the chemical distribution of iron, the defect appears to be a ring-shaped structure with a broad belly in the upper left corner of the image. Also outside the main defect there are some smaller dark spots indicating localized deficiencies of iron. The image at the O K-edge (Fig. 5(b)) reveals that most of these dark areas are in fact holes in the magnetite film through which the MgO substrate with its high oxygen signal becomes visible. This is also true for the main defect, in particular, at the top and the bottom of the image.

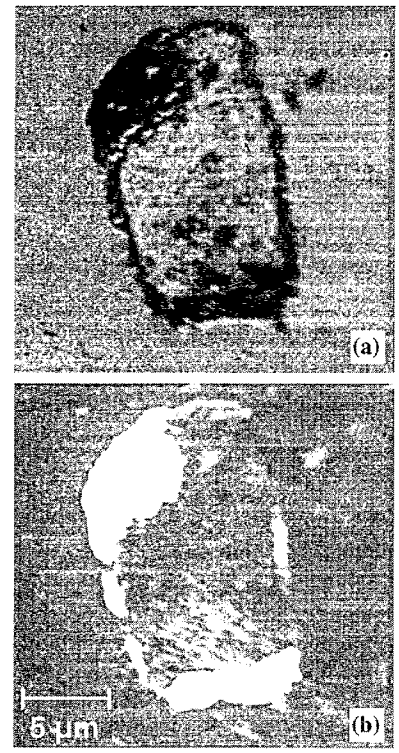

Fig. 5. Elemental mapping of the Fe_3O_4 inhomogeneity island on MgO, shown in Fig. 3. (a) Result of the pixel-by-pixel subtraction of the micrographs taken at the Fe L_3 edge and its "background" (5 eV below). (b) Corresponding difference image at the O K-absorption edge. The difference images (a) and (b) thus emphasize the spatial distribution of Fe and O, respectively.

Some comments must be given concerning the lateral resolution possible when using excitation with soft X-rays. At high photon energies (much larger than the work function) it must be taken into

account that a wide electron kinetic energy distribution generally tends to diminish the maximum achievable spatial resolution. In practice, a well defined electrostatic field is applied between the sample and the outermost surface of the objective, and hence the sample is an integral part of the electrostatic lens system of the PEEM. The strength and shape of this field is critical for the resolution. In the ideal case all photoelectrons should start with zero kinetic energy when penetrating through the surface; then all electrons will be accelerated towards the objective by means of the applied field. Excess excitation energy, however, which exceeds the value necessary for electrons to just leave the surface, will be converted into electron kinetic energy (this is true for both primary and secondary electrons). The amount and direction of the corresponding electron momentum will alter the electron trajectories and thus influence the focusing properties of the objective (chromatic and spherical aberrations). When the high signal of secondary electrons is used for imaging as described above, the width of the energy distribution can be as large as 10 eV (FWHM of the distribution is given by $\sim 2.2 \cdot \Phi$, with Φ being the work function [28]). A proper choice of the size of the contrast aperture and the actual settings of the electrostatic fields within the optics may reduce the width of the distribution somewhat, but still the lateral resolution will be degraded to typically 250 nm.

The effect of wide electron kinetic energy distributions on the achievable spatial resolution due to chromatic aberrations of the electron optics can in principle only be counteracted by introducing an imaging energy filter into the PEEM. As a further advantage, such an energy filter will also enable new modes of operation, for example, imaging with direct photoelectrons or Auger electrons. The drawback, of course, will be a significant loss in signal (and thus longer acquisition times), because the transmission characteristics of the PEEM electron-optical column favors electrons with low kinetic energy.

5. Investigating magnetism with a PEEM

A very interesting application for photoelectron emission microscopy which is currently receiving wide attention is the analysis of magnetic microstructures. Progress in this field is driven by the growing demand for mass storage media with enhanced storage capacity. As a consequence, the lateral dimension of an individual information unit (''bit'')—being essentially a small region with uniform magnetization, i.e. a magnetic domain—written into the magnetic storage material has dropped significantly to present values of well below 1 μm. Characterizing this kind of magnetic microstructure therefore requires a probe with a lateral resolution of 100 nm and better. This circumstance already poses a problem to the classical light-optical methods, such as Kerr microscopy [57], because they are diffraction-limited. Well-established electron-based methods with their superior lateral resolution, such as Lorentz microscopy [58], scanning electron microscopy with spin polarization analysis (SEMPA) [59], or spin-polarized low energy electron microscopy (SPLEEM) [60] are better suited for this particular purpose.

Besides the aspect of resolution, however, there is another important issue. The materials used in magnetic storage technology are either intermetallic compounds, alloys, or multilayers constituting of different chemical species. In order to understand the magnetic behavior of the whole system it is therefore mandatory to determine the magnetic contribution from each of its constituents. This calls for elemental specificity in the magnetic imaging procedure which none of the above techniques can provide. Nevertheless, as we have demonstrated in Section 3 and Section 4, elemental specificity becomes a key feature of photoelectron emission microscopy if the photon energy is tuned to the excitation of a core electronic state. Given a suitable magnetic contrast mechanism, photoemission microscopy will therefore offer a unique combination of lateral resolution, chemical selectivity, and magnetic sensitivity. The resulting experimental technique may be called ''magnetic spectromicroscopy''.

5.1. Magnetic contrast mechanisms

In order to have magnetic sensitivity in an imaging procedure an appropriate contrast mechanism is needed. More specificly, this contrast mechanism must translate the lateral distribution of the local magnetization vector **M** into a signal which can then be

further processed by the instrument. In SEMPA one exploits the fact that both magnitude and direction of the local magnetization are reflected in the spin polarization vector **P** of the emitted low-energy secondary electrons [59]. Thus, by analyzing the lateral distribution of the secondaries with respect to the electron spin one obtains a map of the magnetization vector **M**. In Lorentz microscopy the electron beam traversing the material experiences a Lorentz force due to the local magnetization. As a consequence it will be slightly deflected giving rise to a modulation of the intensity distribution behind the sample which contains the magnetic information [58]. Both approaches are not really manageable in a PEEM. A spin polarization detector involves significant technical efforts and reduces the signal left for imaging by 2–3 orders of magnitude relative to the incoming beam. A sizable contrast from Lorentz deflection requires strong magnetic fields which may have an unwanted influence on the overall imaging capabilities of the instrument. Therefore, a new contrast mechanism is needed.

The most important step towards high-resolution magnetic spectromicroscopy came with the recent discovery of magnetic dichroism [61,62]. Phenomenologically, magnetic dichroism describes the observation that the magnitude and structure of a photoexcitation spectrum may depend in a characteristic manner on the orientation of the magnetization **M** relative to the polarization vector of the incoming light. This is true for both photoabsorption and photoemission processes. In the latter case also the emission direction of the photoelectrons, **k**, and the crystallinity of the sample turn out to be important parameters [63]. The physical basis for magnetic dichroism is an ''interference'' of spin-dependent photoexcitation processes during the optical transition. These processes are governed by the exchange interaction and the spin–orbit coupling in the occupied and unoccupied electronic states involved in the optical excitation.

The most intuitive access to the physical principles of magnetic dichroism can be gained by the discussion of magnetic circular dichroism (MCD) in photoabsorption from the $L_{2,3}$ edges. In this case, the effects due to spin–orbit coupling and exchange interaction can be—to a good approximation—attributed to different electronic levels. We use circularly polarized soft X-rays to excite an electron from the 2p shell of a ferromagnet, say, iron. In an atomic model, the excited electron has a well-defined spin character which is determined only by the direction of the photon spin (or equivalently, the light helicity). In other words, the spin ζ of the excited electron is either parallel or antiparallel to the wavevector **q** of the incident photon. The 2p shell is subject to a considerable spin–orbit interaction and therefore split into $2p_{3/2}$ and $2p_{1/2}$ levels. For the same helicity of the exciting radiation, the spin-polarization of the electrons originating from the $2p_{3/2}$ and $2p_{1/2}$ levels is of opposite sign. This spin-selective excitation of electrons requires the spin–orbit interaction as an essential ingredient and is well-known as ''optical spin orientation'' in both atomic and solid state physics. For completeness, we note that the 2p states may exhibit a further splitting into magnetic sublevels m_J due to the exchange interaction [64]. Because the splitting is small we can neglect it to first order approximation in the present case. It becomes very important, however, if magnetic circular dichroism in direct photoemission is concerned.

In an absorption process, the electrons are excited into the unoccupied section of the density of states below the vacuum level. In a ferromagnet, the density of states is different for spin-up and spin-down electrons, being the origin of the magnetic moment. The density of states is made up predominantly from the d-like valence electrons. The spin-splitting comes about by the exchange interaction and the fact that the electronic system can find a state of lower total energy if the spins are oriented parallel. As a consequence there is an imbalance in the occupied states resulting in more occupied spin-up (majority) states than spin-down (minority) states. In turn, we have more empty minority than majority spin states. The spatial orientation of the spin quantization axis is given by the sample magnetization **M** (majority spin antiparallel, minority spin parallel to **M**).

Now consider a situation in which the two spin quantization axes defined by **q** and **M** are collinear. A spin-up electron excited from a 2p level then directly corresponds to a majority-spin electron in the ferromagnet. Since the spin is preserved during the optical excitation, the transition can only take place into an unoccupied majority spin state. Because

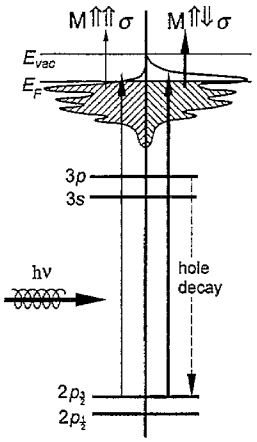

Fig. 6. Principle of magnetic circular dichroism in absorption at the $L_{2,3}$ edge.

the majority spin DOS accessible is small the transition probability is small, too. On the contrary, the transition probability for a minority spin electron is higher, because the corresponding unoccupied DOS is larger (Fig. 6). Measuring the absorption cross-section will therefore show a marked difference for the excitation of the same level with light of opposite helicity. This is the essential meaning of magnetic circular dichroism. The effect exhibits the opposite sign for the other spin–orbit split level. It also changes sign upon a magnetization reversal, because the definition of majority and minority spin states depends only on the relative orientation of **M** and ζ (or equivalently, **q**).

The effect of magnetic dichroism may also be observed in the secondary electrons (total or partial yield) being emitted after the absorption process. The excitation of a 2p electron creates a core hole in the 2p shell. The core hole then decays within a certain lifetime either due to the emission of fluorescence radiation or due to an Auger process. In the latter case, the dichroism can be directly measured in the Auger electron yield [65]. The Auger electron in turn has a relatively high kinetic energy and will generate a cascade of inelastically scattered secondary electrons during its travel through a solid. Therefore also the secondary electrons show a magneto-dichroic signal. Since low-energy secondary electrons contribute most to the signal measured with a PEEM, this magnetic dichroism is the appropriate contrast mechanism needed for magnetic domain imaging [51]. The effect becomes large for the L-edges in the 3d transition metals [66].

In the following examples we will restrict ourselves to magnetic circular dichroism in the soft X-ray regime as a contrast mechanism. We wish to emphasize, however, that there is a large variety of magneto-dichroic effects which can be employed as contrast mechanisms in a photoemission microscope. Several aspects are important in this respect. First, magnetic dichroism is not limited to absorption processes. There are magneto-dichroic phenomena in direct photoemission as well, although the dichroic signals are smaller than in an absorption processes [62]. In addition, the electron quasi-momentum **k** becomes an important parameter leading to complex angular dependencies. These phenomena are therefore referred to as magnetic dichroism in the angular distribution of photoelectrons (MDAD). Magnetic domain imaging on the basis of MDAD has already been demonstrated [67]. Second, magnetic dichroism occurs not only with circularly but also with linearly polarized light (and is therefore observable also with unpolarized light), in both photoemission [68,69] and photoabsorption [70]. Third, magnetic dichroism appears whenever the electronic levels involved in the optical transition are influenced by spin–orbit coupling and exchange interaction. Consequently, one also finds magnetic dichroism in the valence bands [69,71,72]. Whether or not a particular magneto-dichroic effect will be useful as a contrast mechanism, depends to a large extent on the details of the experiment (geometry, magnetization direction, light polarization, excitation energy, etc.).

5.2. Single-crystal surfaces

For demonstrating the capabilities of a magnetic spectromicroscopy using PEEM in combination with circularly polarized synchrotron radiation, we have chosen an Fe(100) whisker surface. Fig. 7(a) shows a 70×70 μm area of the surface. In order to obtain this image, the following procedure has been applied. First, two images have been recorded with the photon energy tuned to the L_2 and L_3 edge of iron. These images contain a mixture of magnetic information and other contrast mechanisms (e.g. of chemical or topographic origin). In order to separate the magnetic contribution and obtain a quantitative measure, an

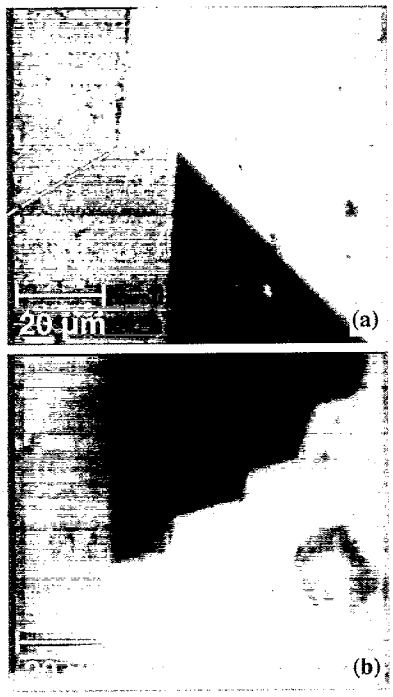

Fig. 7. Magnetic domain pattern obtained by means of X-ray magnetic circular dichroism from an "L"-shaped Fe(100) whisker. Pixel-by-pixel image subtraction of micrographs taken at photon energies tuned to the Fe L_3 and L_2 absorption edges, respectively. Light incidence from the lower left. High contrast is visible at 180° domain walls. (a) Difference image acquired at the inner elbow corner of the whisker. (b) Image acquired at the vertical leg of the whisker. The "facetted" 180° domain wall is aligned parallel to the whisker leg.

asymmetry image is formed according to

$$A(x,y)=\frac{I_{L_3}(x,y)-I_{L_2}(x,y)}{I_{L_3}(x,y)+I_{L_2}(x,y)} \qquad (2)$$

For iron the asymmetry $A(x,y)$ is large enough ($\approx 21\%$ upon magnetization reversal) for the magnetic contrasts to be seen in each individual image I_{L_2} and I_{L_3}. In a gray-scale representation Fig. 7(a) essentially exhibits three different levels. These three levels, however, correspond to four different orientations of the magnetization vector (induced by the four-fold symmetry of the surface). The sample had been oriented such that two of the four possible directions of **M** were oriented parallel and antiparallel to **q**. The other two directions are orthogonal to **q** and therefore their MCD signal disappears resulting in the intermediate gray level. The arrows indicate the orientation of **M** in each domain as deduced from the contrast. From this we find two different domain boundaries in the image, namely so-called 180°- and 90°-walls. The latter runs almost vertically across the whole image and forms the step-like structure in the center. Starting from the edge of the step there is a very faint line, the position of which is marked by the broken line in Fig. 7(a). This line indicates the presence of another 180°-wall. In order to understand how this contrast arises we recall that in the bulk a 180°- or Bloch-wall is characterized by a rotation of the magnetization vector around an axis perpendicular to the wall plane. At the surface, however, this behavior changes and the wall becomes Neél-like, i.e. the magnetization vector rotates around an axis parallel to the wall plane and normal to the surface [73,74]. This way, a component of **M** normal to the surface is avoided and the stray field is minimized. As a consequence of its Neél-type behavior within the wall the magnetization vector has a component normal to the wall plane and thus along **q**. This component can be picked up in the experiment and gives rise to a measurable contrast. In this particular situation where we cannot see the domains themselves, we are sensitive to the domain wall only.

The image reproduced in Fig. 7(b) is taken from a different location on the same whisker surface. It shows two oppositely magnetized domains which are separated by a complex arrangement of domain walls which form a staircase-like pattern.

The magnetic microstructure depends very sensitively on the crystallinity of the specimen. This is shown in the next example. The images in Fig. 8 have been recorded from a $Fe_{50}Pt_{50}(100)$ single crystal surface using the dichroism at the Fe $L_{2,3}$ edges. Again, the four-fold symmetry of the surface implies four mutually orthogonal directions of the magnetization vector within the surface. As in the case of the Fe-whisker the sample is oriented such that two of the four possible directions for **M** are normal to the incoming light resulting in three contrast levels. There are two different types of domain patterns which can be found on the surface of this particular crystal. In Fig. 8(a) we see a rather regular arrangement of domains with square and rectangular shapes. The domain boundaries run along low index crystalline directions. Only a few 10 μm away from

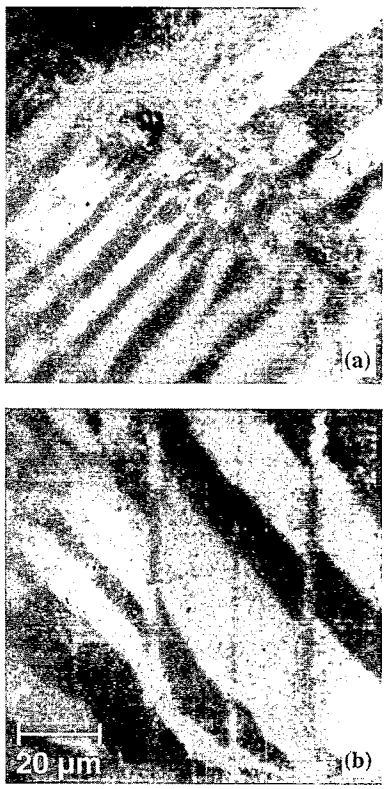

Fig. 8. Magnetic domain patterns from two different locations on an $Fe_{50}Pt_{50}$ alloy single crystal surface. The images show the influence of the sample crystallinity on the magnetic microstructure.

the position at which Fig. 8(a) was captured, we found a completely different domain pattern (Fig. 8(b)). The domains are stripe-like with curved boundaries. This behavior is attributed to the influence of misaligned grains, which change the local orientation of the magnetically easy directions in space.

The above imaging results from magnetic single crystal surfaces should also be discussed with respect to possible time-resolved experiments. In fact, the magnetic dichroism at the Fe $L_{2,3}$-edges is so strong that the image can be easily observed by means of a simple TV camera. This opens up the possibility to study magnetic phenomena at surfaces and in ultrathin film systems in real-time. Of interest are, for example, variations of the magnetic microstructure as a function of temperature, film thickness, or adsorbate coverage. Other applications include the decay of a magnetized state after switching of an external field (''magnetic after-effect'').

5.3. Magnetism in a microstructured sample

In order to illustrate the combination of chemical and magnetic information that can be obtained with a PEEM we come back to the microstructured Permalloy sample introduced in Section 3. The example is in our case an array of Permalloy ($Fe_{19}Ni_{81}$) squares on a Si(100) substrate.

The magnetic image obtained at the Fe $L_{2,3}$ edges shows again three levels of contrast (Fig. 9(a)). In each square we observe a characteristic pattern

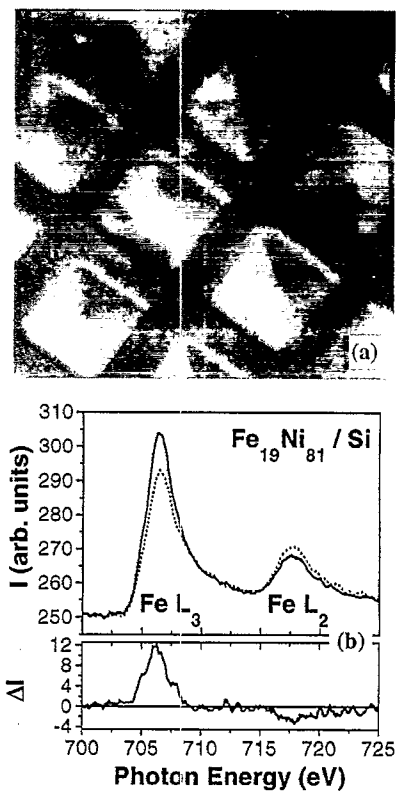

Fig. 9. X-ray circular magnetic dichroism microscopy and microspectroscopy from the permalloy microstructure on silicon shown in Fig. 2 using left hand circularly polarized light. (a) Pixel-by-pixel difference image of the microstructure as the result of subtraction of microimages taken at the Fe L_3 and L_2 absorption edges. It reveals the pattern of magnetic domains contained in each of the $Fe_{19}Ni_{81}$ squares. Light incidence from the lower left. (b) Spectra taken from small spots located on the dark and bright domains within one of the $Fe_{19}Ni_{81}$ squares (full and dashed curve, respectively). The top panel shows the absorption intensity as acquired from microareas with opposite magnetization for the same photon helicity. The bottom line shows the difference signal.

composed of four triangles. The magnetization vector in the triangles is oriented such that we obtain a flux closure, indicating that the system tends to minimize the magnetic stray field. The pattern therefore contains two 90°-walls, running along the diagonals of the square and intersecting each other in the center. An exception from this behavior is the square in the center of the image. Probably due to a defect in the film the magnetic microstructure in this square is more complicated. Basically the same information can be obtained by imaging the Ni signal. Note that the asymmetry image is also chemically selective, because it only contains the information from the Fe (or alternatively Ni) lines. One therefore combines magnetic sensitivity and chemical selectivity in the imaging process.

In analogy to Section 3, we can also perform magnetic microspectroscopy studies. By following the intensity in selected areas of the image as a function of photon energy, one should obtain a magnetic dichroism spectrum on the μm scale. This is shown in Fig. 9(b), which displays the $L_{2,3}$ absorption spectra simultaneously recorded at the position of a ''dark'' and a ''bright'' triangular domain in one of the Permalloy squares in Fig. 9(a). The signals from the two oppositely magnetized domains (top panel in Fig. 9(b)) show a clear difference in the peak heights of the L_3 and L_2 absorption line. The difference of the two spectra (bottom panel in Fig. 9(b)) is larger for the L_3 edge and changes sign at the L_2 edge. The spectra agree with those obtained by means of conventional macroscopic techniques [75,76]. In fact, we note that the spectral resolution is very good, because the energy spread of the light within the selected area is very small. As an advantage of this microscopy technique, several regions within the image can be measured simultaneously, thereby eliminating the influence of instabilities of the light source which would otherwise impair the magneto-dichroic measurements. Furthermore, chemical and magnetic information are obtained at the same time (see Section 3).

6. Outlook: micro-ESCA energy filter

Although micro-XAS as described in Section 3 is a very simple but highly effective method of elemental microanalysis, it has an important disadvantage as it requires X-ray radiation continuously tunable over an energy range of several hundred eV. Hence, μ-XAS can only be performed at synchrotron radiation sources. This may be a drawback for those microscopists who need an all-day access to a laboratory instrument.

The standard method for elemental microanalysis is the EDX (energy dispersive X-ray detector) of an SEM. As a result of the low cross-section of the electron-induced fluorescence signal, this detector is comparably slow and requires high primary current densities in the electron microprobe. Thus, sample damage is a major problem, in particular, for unstable and delicate species such as biological objects, polymer films, adsorbate layers etc. Moreover, this microprobe must principally employ relatively high primary beam energies. Then, the problem of ''blooming'' becomes important, i.e. an increase of the volume within the sample which contributes to the signal (due to scattering processes of the primary and secondary electrons) which causes a degradation of the spatial resolution. For the same reason EDX, in particular, is not very surface sensitive. It is a powerful method for quantitative chemical analysis of stable species with a thickness of many atomic layers, but not for fragile thin samples.

In spectroscopy experiments, the standard method for element analysis is ESCA (electron spectroscopy for chemical analysis). It is a fast and powerful technique normally utilizing laboratory X-ray sources. ESCA requires only one fixed energy (typically Al Kα or Mg Kα at 1400 eV or 1253 eV, respectively), because as fingerprints serve the kinetic energies E_{kin} of the photoelectrons measured by means of an electron spectrometer. These are a direct measure for the atomic binding energies E_B by making use of the energy conservation law

$$h\nu = E_B + \Phi + E_{kin} \tag{3}$$

with Φ being the work function of the sample surface. Consequently, this technique is a major step towards laboratory X-PEEM, but it requires an electron energy analyzer in the microscope. In addition, it requires a high-brilliance laboratory X-ray source for illumination of the small field of view (in the range between 1 μm and several 100 μm). Conventional X-ray tubes have a large source size and

therefore an insufficiently low photon density on the sample. A promising approach is the combination of special focusing multilayer mirrors having very high reflectivities in the soft X-ray region with a laser-induced microplasma X-ray source. We will examine this laboratory source for X-PEEM in the near future.

The "ideal" approach to an ESCA-based X-PEEM is to employ an imaging energy filter which allows element-specific imaging when the bandpass of the filter is tuned to a corresponding ESCA line. Two such instruments have been built [46,77], a third and highly sophisticated one is under construction (a development initiated by H. Rose, see [78]). In principle this approach has no basic disadvantages. However, in the present stage of development the complexity of these instruments restricts their use to a few specialists only [38].

On our way towards a laboratory X-PEEM we have started with an easy-to-use "low-budget" solution. Instead of inserting a highly corrected imaging filter, we added a simple electron energy analyzer of a well-established design (FOCUS SHA 50) to the IS-PEEM. The arrangement is illustrated in Fig. 10. The non-imaging analyzer is located in the column

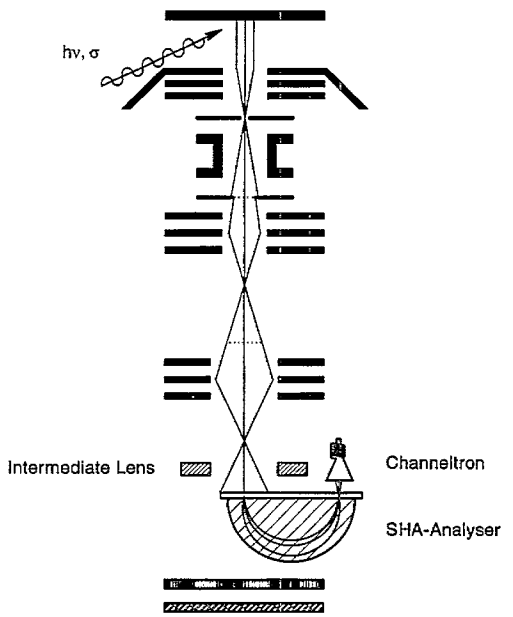

Fig. 10. Schematics of the IS-PEEM equipped with the Micro-ESCA energy filter.

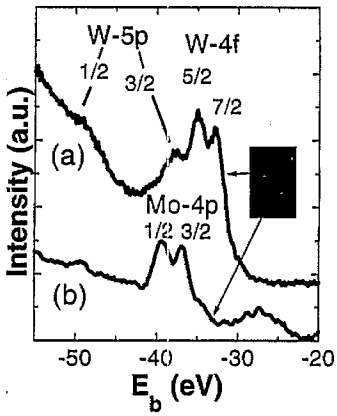

Fig. 11. First results of elemental analysis via microspot-ESCA on a tungsten-molybdenum sample surface. This technique operates at a fixed photon energy, here at $\hbar\omega$ = 95 eV. Micro-ESCA spectra from a tungsten (a) and a molybdenum region (b) on the sample, showing the resolved tungsten 5p and 4f, and the molybdenum 4p emission, respectively.

behind the second projective lens. The SHA 50 is a simulated hemispherical condenser [79]. For the present purpose it has the specific advantage that its outer sphere is constructed from a highly transparent grid with a very fine mesh. In the imaging mode the electrons can pass this grid on the way to the screen. Thus the switching between imaging and spectroscopy requires only a shift of the entrance slit of the analyzer into its position (via a linear motion feedthrough) and application of the analyzer voltages. Microspot selection is facilitated by closing the variable iris aperture in the intermediate image plane after the region of interest has been centered by using the piezomotor-driven *x/y* stage and/or the electrostatic *x/y* deflector in the column. Behind the exit slit of the analyzer the electron signal is detected by a channeltron multiplier in pulse-counting mode.

A typical result from the first testing period is shown in Fig. 11 (this experiment was performed in cooperation with U. Kleineberg, D. Menke and U. Heinzmann from the Universität Bielefeld, Germany). The sample consisted of a molybdenum strip on a tungsten single crystal surface. It was illuminated with 95 eV photons obtained by focusing the direct radiation from an undulator beamline (BESSY U2) by means of a multilayer mirror [80] into a 1.5 mm spot on the sample. The selective reflectivity of the multilayer mirror limits the band width

of the incident radiation to a range of 1...2 eV. The spectra were recorded from areas with approximately 200 μm dia. The spectrum from the tungsten area taken with $\hbar\omega$ = 95 eV shows photoemission from the 5p and 4f levels, with the respective spin–orbit splittings clearly resolved. These states have been identified according to their characteristic binding energy. In the same range of binding energies one also finds photoemission from the Mo 4p levels which is seen in the second spectrum obtained from the molybdenum strip. These first results demonstrate the instruments capability to record photoemission spectra with a good signal-to-noise ratio from microscopic regions down to a few μm.

7. Summary

In particular the last example in Section 6 underlines the importance of an advanced design in order to exploit the versatility of an immersion lens electron microscope for studies in surface physics. Access to the entire potential of a PEEM, however, requires operating the instrument at a synchrotron radiation facility. In this case one can use the full spectrum of contrast mechanisms which are of interest in investigations of surface morphology, surface chemistry, and surface magnetism. Nourished by the growing need for analytical techniques on a mesoscopic scale, photoemission microscopy is developing into an important tool in these fields, either as a stand-alone instrument, or in combination with other microscopy techniques which allow access to other length scales, e.g. scanning tunneling or scanning electron microscopy.

Acknowledgements

We are indebted to A. Wadas and R. Wiesendanger (Inst. f. Angewandte Physik, Universität Hamburg, Germany) for fabricating the Permalloy microstructure on silicon. Thanks are due to J.M. Gaines, R.M. Jungblut (both Philips Research Laboratories, Eindhoven, Netherlands) and F.U. Hillebrecht (Inst. f. Angewandte Physik, Universität Düsseldorf, Germany) for making available the Fe_3O_4 sample. The Fe(100) whiskers have been generously supplied by B. Heinrich (Surface Physics Laboratory, Simon Fraser University, Burnaby, Canada). Part of this work was supported by the BMBF under grants 05644EFA5 and O5644UMA7.

References

[1] E. Brüche, Z. Phys. 86 (1933) 448.
[2] H. Bethge, T. Krajewski, O. Lichtenberger, Ultramicroscopy 17 (1985) 21.
[3] M. Mundschau, E. Bauer, W. Swiech, J. Appl. Phys. 65 (1989) 581.
[4] M. Mundschau, E. Bauer, W. Swiech, J. Appl. Phys. 65 (1989) 4747.
[5] E. Bauer, M. Mundschau, W. Swiech, W. Telieps, Ultramicroscopy 31 (1989) 49.
[6] M. Mundschau, E. Bauer, W. Swiech, Surface Sci. 203 (1988) 412.
[7] M. Mundschau, E. Bauer, W. Swiech, Catal. Lett. 1 (1988) 405.
[8] M. Mundschau, M.E. Kordesch, B. Rausenberger, W. Engel, A.M. Bradshaw, E. Zeitler, Surface Sci. 227 (1990) 246.
[9] W. Engel, C.S. Rastomjee, A.K. Schmid, B. Rausenberger, A.M. Bradshaw, E. Zeitler, in B. Jouffrey, C. Colliex (Eds.), Electron Microscopy, Editions de Physique, Les Ulis, 1994, p. 194.
[10] J. Lauterbach, G. Haas, H.H. Rotermund, G. Ertl, Surface Sci. 294 (1993) 116.
[11] H.H. Rotermund, Physica Scripta T49 (1993) 549.
[12] J. Lauterbach, H.H. Rotermund, Surface Sci. 311 (1994) 231.
[13] A. Garcia, M.E. Kordesch, J. Vac. Sci. Technol. A 13 (1995) 1396.
[14] G. Veser, F. Esch, R. Imbihl, Catal. Lett. 371 (1992) 13.
[15] H.H. Rotermund, S. Nettesheim, A.v. Oertzen, G. Ertl, Surface Sci. Lett. 275 (1992) L645.
[16] A.v. Oertzen, H.H. Rotermund, S. Nettesheim, Chem. Phys. Lett. 199 (1992) 131.
[17] A.v. Oertzen, H.H. Rotermund, S. Nettesheim, Surface Sci. 311 (1994) 322.
[18] M. Ondrejcek, W. Stenzel, H. Conrad, V. Chab, Z. Chvoj, W. Engel, A.M. Bradshaw, Chem. Phys. Lett. 215 (1993) 528.
[19] M. Ondrejcek, V. Chab, W. Stenzel, M. Snabl, H. Conrad, A.M. Bradshaw, Surface Sci. 331–333 (1995) 764.
[20] M. Snabl, M. Ondrejcek, V. Chab, W. Stenzel, H. Conrad, A.M. Bradshaw, Surface Sci. 546 (1996) 352.
[21] J.D. Shovlin, M.E. Kordesch, D. Dunham, B.P. Tonner, W. Engel, J. Vac. Sci. Technol. A 13 (1995) 1111.
[22] C. Wang, J. Macaulay, J.D. Shovlin, M.E. Kordesch, Diamond and Related Materials 3 (1994) 1066.
[23] A. Garcia, C. Wang, M.E. Kordesch, Appl. Phys. Lett. 61 (1992) 2984.
[24] H.O. Griffith, G.F. Rempfer, Adv. Opt. Electr. Microsc. 10 (1987) 269.

[25] G.F. Rempfer, W.P. Skoczylas, O.H. Griffith, Ultramicroscopy 36 (1991) 196.
[26] G.B. Birell, K.K. Hedberg, D.L. Habliston, O.H. Griffith, Ultramicroscopy 36 (1991) 235.
[27] B.P. Tonner, J. Phys. Colloq. (France) C9 (1994) 407.
[28] B.P. Tonner, D. Dunham, Nucl. Instr. Meth. A347 (1994) 436.
[29] W. Gudat, C. Kunz, Phys. Rev. Lett. 29 (1972) 169.
[30] B.P. Tonner, G.R. Harp, S.F. Koranda, J. Zhang, Rev. Sci. Instrum. 63 (1992) 564.
[31] B.P. Tonner, Nucl. Instr. Meth. A291 (1990) 51.
[32] G. Lilienkamp, E. Bauer, Private communication, 1995.
[33] L.H. Veneklasen, Rev. Sci. Instrum. 63 (1992) 5513.
[34] S. Lanio, H. Rose, D. Krahl, Optik 73 (1986) 56.
[35] D. Krahl, H. Rose, in Energy-Filtering Transmission Electron Microscopy, Springer, Berlin, 1995, p. 110.
[36] E. Umbach, Physica B208/209 (1995) 193.
[37] K. Tsuno, Rev. Sci. Instrum. 64 (1993) 659.
[38] G.K.L. Marx, M.D.v. Przychowski, B. Krömker, C. Ziethen, G. Schönhense, Forsch. Johannes-Gutenberg-Univ. Mainz, (1994) 26.
[39] G.K.L. Marx, V. Gerheim, G. Schönhense, 1996, this issue.
[40] E. Bauer, Ultramicroscopy 36 (1991) 52.
[41] B.P. Tonner, G.R. Harp, J. Vac. Sci. Technol. A 7 (1989) 1.
[42] G.R. Harp, B.P. Tonner, Z.L. Han, J. Vac. Sci. Technol. A 8 (1990) 2556.
[43] G. DeStasio, S.F. Koranda, B.P. Tonner, G.R. Harp, D. Mercanti, M.T. Ciotti, G. Margaritondo, Europhys. Lett. 19 (1992) 655.
[44] G. DeStasio, S. Hardcastle, S.F. Koranda, B.P. Tonner, M.T. Ciotti, D. Mercanti, P. Perfetti, G. Margaritondo, Phys. Rev. E 47 (1993) 2117.
[45] G. DeStasio, D. Dunham, B.P. Tonner, D. Mercanti, M.T. Ciotti, A. Angelini, C. Coluzza, P. Perfetti, G. Margaritondo, NeuroReport 4 (1993) 1175.
[46] B.P. Tonner, D. Dunham, T. Droubay, J. Kikuma, J. Delinger, E. Rotenburg, A. Warwick, J. Electron Spectrosc. Relat. Phenom. 75 (1995).
[47] J. Delinger, E. Rotenberg, T. Warwick, G. Visser, J. Nordgren, J.-H. Gua, P. Skytt, S.D. Kevan, K.S. McCutcheon, D. Shuh, J. Bucher, N. Edelstein, J.G. Tobin, B.P. Tonner, Rev. Sci. Instrum. 66 (1995) 1342.
[48] Y. Hwu, C.Y. Tung, J.Y. Pieh, S.D. Lee, P. Almeras, F. Gozzo, H. Berger, G. Margaritondo, G.D. Stasio, D. Mercanti, M.T. Ciotti, Nucl. Instr. Meth. A361 (1995) 349.
[49] G.H. Fecher, Y. Hwu, W. Swiech, Surface Science, 1996, in press.
[50] G. Margaritondo, Y. Hwu, Appl. Surf. Sci. 92 (1996) 273.
[51] J. Stöhr, Y. Wu, M.G. Sarmant, B.D. Hermsmeier, G. Harp, S. Koranda, D. Dunham, B.P. Tonner, Science 259 (1993) 658.
[52] Y. Wu, S.S.P. Parkin, J. Stöhr, M.G. Samant, B.D. Hermsmeier, S. Koranda, D. Dunham, B.P. Tonner, Appl. Phys. Lett. 63 (1993) 263.
[53] Ultramicroscopy 36 (1991).
[54] G. Margaritondo, Scanning Microscopy 9 (1995) 949.
[55] K. Grzelakowski, E. Bauer, Rev. Sci. Instrum. 67 (1996) 742.
[56] J. Giergiel, H. Hopster, J.M. Lawrence, J.C. Hemminger, J. Kirschner, Rev. Sci. Instrum. 66 (1995) 3475.
[57] J. Kranz, A. Hubert, Z. Angew. Phys. 15 (1963) 220.
[58] J.N. Chapman, J. Phys. D 17 (1984) 623.
[59] H.P. Oepen, J. Kirschner, Scanning Microscopy 5 (1991) 1.
[60] M. Altmann, H. Pinkvos, J. Hurst, H. Poppa, G. Marx, E. Bauer, Mat. Res. Soc. Symp. Proc. 232 (1991) 125 .
[61] G. Schütz, W. Wagner, W. Wilhelm, P. Kienle, R. Zeller, R. Frahm, G. Materlik, Phys. Rev. Lett. 58 (1987) 737.
[62] L. Baumgarten, C.M. Schneider, F. Schäfers, H. Petersen, J. Kirschner, Phys. Rev. Lett. 65 (1990) 492.
[63] D. Venus, L. Baumgarten, C.M. Schneider, C. Boeglin, J. Kirschner, J. Phys.: Cond. Matt. 5 (1993) 1239.
[64] H. Ebert, L. Baumgarten, C.M. Schneider, J. Kirschner, Phys. Rev. B 44 (1991) 4406.
[65] C.M. Schneider, K. Holldack, M. Kinzler, M. Grunze, H.P. Oepen, F. Schäfers, H. Petersen, K. Meinel, J. Kirschner, Appl. Phys. Lett. 63 (1993) 2432.
[66] C.T. Chen, F. Sette, Y. Ma, S. Modesti, Phys. Rev. B 42 (1990) 7262.
[67] C.M. Schneider, Z. Celinski, M. Neuber, C. Wilde, M. Grunze, K. Meinel, J. Kirschner, J. Phys.: Cond. Matt. 6 (1994) 1177.
[68] C. Roth, F.U. Hillebrecht, H.B. Rose, E. Kisker, Phys. Rev. Lett. 70 (1993) 3479.
[69] M. Getzlaff, C. Ostertag, G.H. Fecher, N.A. Cherepkov, G. Schönhense, Phys. Rev. Lett. 73 (1994) 3030.
[70] F.U. Hillebrecht, T. Kinoshita, D. Spanke, J. Dresselhaus, C. Roth, H.B. Rose, E. Kisker, Phys. Rev. Lett. 75 (1995) 2224.
[71] C.M. Schneider, M.S. Hammond, P. Schuster, A. Cebollada, R. Miranda, J. Kirschner, Phys. Rev. B 44 (1991) 12066.
[72] H.B. Rose, C. Roth, F.U. Hillebrecht, E. Kisker, Solid State Commun. 91 (1994) 129.
[73] H.P. Oepen, J. Kirschner, Phys. Rev. Lett. 62 (1989) 819.
[74] M.R. Scheinfein, J. Unguris, R.J. Celotta, D.T. Pierce, Phys. Rev. Lett. 63 (1989) 668.
[75] C.T. Chen, Y.U. Idzerda, H.-J. Lin, N.V. Smith, G. Meigs, E. Chaban, G.H. Ho, E. Pellegrin, F. Sette, Phys. Rev. Lett. 75 (1995) 152.
[76] W.L. O'Brien, B.P. Tonner, G.R. Harp, S.S.P. Parkin, J. Appl. Phys. 76 (1994) 6462.
[77] E. Bauer, T. Franz, C. Koziol, G. Lilienkamp, T. Schmidt, in R. Rosei (Ed.), Recent Advances in LEEM/PEEM for Structural and Chemical Analyses, Kluwer, Dordrecht, 1996.
[78] D. Preikszas, Ph.D. Thesis, Universität Darmstadt, Unpublished.
[79] K. Jost, J. Phys. 12 (1979) 1006.
[80] B. Schmiedeskamp, A. Kloidt, H.-J. Stock, U. Kleineberg, T. Döhring, M. Pröpper, S. Rahn, K. Hilgers, B. Heidemann, T. Tappe, U. Heinzmann, M. Krumney, P. Müller, F. Scholze, K.F. Heidemann, Opt. Eng. 33 (1994) 1314.